Physica Medica 65 (2019) 181–190

Contents lists available at ScienceDirect

Physica Medica

journal homepage: www.elsevier.com/locate/ejmp

Original paper

Size-specific dose estimations for pediatric chest, abdomen/pelvis and head CT scans with the use of GATE

Theodora Kostou[a], Panagiotis Papadimitroulas[b], Pavlos Papaconstadopoulos[c], Slobodan Devic[d], Jan Seuntjens[d], George C. Kagadis[a,*]

[a] University of Patras, Department of Medical Physics, Patras, Greece
[b] BioEmission Technology Solutions, R&D Department, Athens, Greece
[c] The Netherlands Cancer Institute, Amsterdam, Netherlands
[d] McGill University, Department of Medical Physics, Montreal, Canada

ARTICLE INFO

Keywords:
CT
External dosimetry
Organ dose
Pediatric
Database
Monte Carlo simulations
GATE
Patient size
Computational phantoms

ABSTRACT

Purpose: The purpose of this study is to create an organ dose database for pediatric individuals undergoing chest, abdomen/pelvis, and head computed tomography (CT) examinations, and to report the differences in absorbed organ doses, when anatomical differences exist for pediatric patients.
Methods: The GATE Monte Carlo (MC) toolkit was used to model the GE BrightSpeed Elite CT model. The simulated scanner model was validated with the standard Computed Tomography Dose Index (CTDI) head phantom. Twelve computational models (2.1–14 years old) were used. First, contributions to effective dose and absorbed doses per $CTDI_{vol}$ and per 100 mAs were estimated for all organs. Then, doses per $CTDI_{vol}$ were correlated with patient model weight for the organs inside the scan range for chest and abdomen/pelvis protocols. Finally, effective doses per dose-length product (DLP) were estimated and compared with the conventional conversion k-factors.
Results: The system was validated against experimental $CTDI_w$ measurements. The doses per $CTDI_{vol}$ and per 100 mAs for selected organs were estimated. The magnitude of the dependency between the dose and the anatomical characteristics was calculated with the coefficient of determination at 0.5–0.7 for the internal scan organs for chest and abdomen/pelvis protocols. Finally, effective doses per DLP were compared with already published data, showing discrepancies between 13 and 29% and were correlated strongly with the total weight ($R^2 > 0.8$) for the chest and abdomen protocols.
Conclusions: Big differences in absorbed doses are reported even for patients of similar age or same gender, when anatomical differences exist on internal organs of the body.

1. Introduction

The number of Computed Tomography (CT) examinations is rapidly increasing due to the continuous technological improvements that allow fast exams and high image quality [1–3]. However CT radiation dose is considered to be higher compared to the rest medical imaging modalities [4]. It is estimated that about 10% of 100 million CT exams per year is performed on patients less than 18 years old [5,6]. Available risk estimates suggest that pediatric CT will result in significantly increased risk of developing radiation-induced malignancies, including leukemia, brain, breast, skin, and thyroid cancer, due to the long life expectation and the rapid cell replication [7–12]. Indicatively for the abdomen and head scans, the estimated life-time increase in cancer mortality risks for 1-year old children are 0.18% and 0.07%, respectively [13]. Also, in a more recent study, it was estimated that for pediatric CT, the life-time risks of leukemia might become 1-in-7500, and brain cancer 1-in-1000 [14].

Accurate estimation of the organ dose after a CT scan is not a simple task. Currently in clinical practice, the volumetric CT dose index ($CTDI_{vol}$), determined in standard-sized cylindrical phantoms in the scan region, and the dose length product (DLP), the product of $CTDI_{vol}$ with scan length, are reported after each CT examination as patient dose indices [15]. In clinical practice, $CTDI_{vol}$ describes the scanner output and does not provide information about patient size. In 2011, size-specific dose estimate (SSDE) was also introduced as a new updated index that takes into account the patient size, affecting the average dose [16–18]. However, this method still induces limitations to predict with accuracy the effective dose because tissue heterogeneity and exact

* Corresponding author at: Department of Medical Physics, School of Medicine, University of Patras, GR 26504, Greece.
E-mail address: gkagad@gmail.com (G.C. Kagadis).

https://doi.org/10.1016/j.ejmp.2019.08.020
Received 16 May 2019; Received in revised form 24 July 2019; Accepted 29 August 2019
Available online 05 September 2019

patient anatomy are not taken into consideration. In addition two CT radiographs are required to measure AP and LAT diameters in order to calculate the SSDE of each patient, increasing the dose in low-dose CT-procedures up to 38% of the total patient dose [19]. Lately, added web-based software, DoseWatch (General Electric Inc., Milwaukee, USA), is able to calculate AP and LR diameters for each examination using projections from the scout view [20,21]. Diagnostic reference levels (DRLs) of $CTDI_{vol}$, DLP and SSDE are available for protocol optimization and management of the doses [22,23].

Shrimpton et al. introduced the effective dose per DLP conversion factors, i.e. k-factors ($mSv\,mGy^{-1}\,cm^{-1}$) with the aid of stylized adult reference models [24] and Monte Carlo simulations [25] to help clinicials calculate doses in a fast manner. Updated k-factors were then developed by other groups [26,27] and later, they were extended for pediatric patients (newborn, 1-, 5-, 10-, and 15-year-old) for several commonly used CT protocols [15,28,29]. New sex- and age-specific conversion factors were generated by Deak et al. for different scanning conditions [30]. Romanyukha et al. updated the existing age-specific k-factors using ICRP reference phantoms [31] and presented new body size-specific k-factors derived from regression functions applied to a large population who underwent chest, AP and CAP [32]. However, the existing k-factors, based on reference phantoms, introduce an important over- or under- estimation of the effective dose in the case of underweight and obese patients.

The effective dose can be directly estimated either by the use of experimental measurements on physical anthropomorphic phantoms [33–35] or faster and more accurately by Monte Carlo simulations using mathematical or voxelized models [36–39]. For the latter, the precise estimation of effective dose from a CT scan requires an detailed description of scanner's technical specifications [40,41] and a large amount of computational phantoms that account for anatomical variations for different type of scan acquisitions. Several organ dose calculators have been developed. The first of them, such as CTDosimetry [42], CTDOSE [43], eXposure [44], and WinDose [45], were based on unrealistic adult stylized phantoms [46,47], with simple geometric shapes instead of organs, introducing significant dosimetry errors (up to 21%) [48]. CT-Expo [49] was based on adult stylized phantoms as well as on the first pediatric models created from tomographic data in the late 1980s [50,51]. The most recent dosimetric packages [52–54] are based on adult and pediatric voxelized phantoms [55–59] to overcome these uncertainties. VirtualDose [60] is the first program that included realistic phantoms that represent patients of different ages, body sizes, body masses, and pregnant females at three gestational stages for different scanners, protocols and tube current modulation (TCM). Later, based on VirtualDose, Gao et al. estimated the effective doses from CT scans of 1250 pediatric oncologic patients with the use of patient-specific information [61].

Except from the development of clinical pediatric dosimetry softwares, several other groups focused their research on the pediatric organ dose estimation [62–75]. In a recent study, the advantage of patient-specific phantoms in comparison with patient-dependent hybrid phantoms, in its ability to predict patient dose with accuracy was addressed by Marshall et al. [76] for pediatric patients undergoing fluoroscopically guided cardiac procedures. Moreover, Stepusin et al. [77] in 2017 concluded that matching a patient to a computational hybrid phantom in a library is superior to matching to a reference phantom.

The aim of this study is to create an organ dose database for pediatric patients undergoing CT exams. The database includes the cases of head, chest and abdomen/pelvis exams using current pediatric protocols. When patient anatomical differences exist, differences in absorbed doses per organ and body type are reported.

2. Materials and methods

2.1. GATE MC platform

A multislice helical CT scanner was modeled using the Geant4 application for tomographic emission (GATE) [78,79]. For this study, GATE v8.0 was used, which is based on Geant4 v10.1. The physical processes are specified by the EMLivermore physics list, which is optimized for the accuracy of electrons and photon physics for low energies and have been widely used for imaging and therapy [80–85]. In all simulations, a production threshold of 0.01 mm was used for all particles. Livermore models are used for photoelectric, Rayleigh and Compton processes, are valid for energies 250 eV to 100 GeV and have replaced the standard model (valid 1 keV to 100 TeV) for low energy physics processes.

The absorbed dose was measured through the deposited energy. The "dose actor" tools were used in GATE to store the deposited energy per voxel. 3D matrices of the deposited energy with certain voxel resolution were created and the relative statistical uncertainty per voxel was calculated for several simulations. The statistical uncertainty ε_k at voxel k, with N being the number of primary events and $d_{k,i}$ the deposited energy in voxel k for primary event i is described in Eq. (1):

$$D_k = \sum_i^N d_{k,i},\ S_k = \sqrt{\frac{1}{N-1}\left(\frac{\sum_i^n d_{k,i}^2}{N} - \left(\frac{\sum_i^n d_{k,i}}{N}\right)^2\right)},\ \varepsilon_k = 100 \times \frac{S_k}{D_k} \tag{1}$$

We calculated the relative statistical uncertainties for all simulations. 10^8 primaries were chosen to keep the uncertainty lower than 5% in all organs of interest.

2.2. CT source model – specifications

GE BrightSpeed Elite 16 Slice scanner is the CT scanner of the study, which offers high resolution imaging at up to 0.35 mm isotropic at an optimized dose. The X-ray tube operates from 80 to 140 kVp with a rotating 7° tungsten target and two focal spots (0.9 mm × 0.7 mm and 1.2 mm × 1.1 mm). The nominal inherent filtration is more than 2 mm of aluminum equivalent thickness.

The initial X-ray energy spectra for a certain kilovoltage peak (kVp) setting was estimated using the Spektr Software, developed by Siewerdsen et al. [86]. The software is based on the Tungsten anode spectral model using interpolating polynomials (TASMIPs) [87], while the approach is completely empirical and based on straightforward interpolation techniques using a modified version of Fewell's measured spectra [88] as a data source. SPEKTR is consisted of Matlab™ library functions, a database of attenuation coefficients, and a user interface, allowing a user to obtain TASMIP spectra with an energy resolution of 1.0 keV from the TASMIP library. The user needs to import the maximum energy, the added filtration, the inherent filtration and the peak-to-valley voltage over the peak voltage (kV Ripple %).

The X-ray source-to-detector distance, the source-to-isocenter distance and the dimensions of inherent and bowtie filters were accurately defined using the manufacturer technical specifications under a non-disclosure agreement (NDA). Fig. 1 depicts the modelling of the GE BrightSpeed-Elite 16 X-ray source.

The spectrum in GATE was inserted using a text file, describing the energy histogram. Then the fan and cone angle were defined. In order to model the rotational and the helical movement of the CT X-ray beam, an extra file was prepared in the GATE simulator. An almost continuous movement of the source was achieved. In order to achieve that, the 360° of one source rotation were divided in 800 steps of 0.45° angle rotation in each step (1.25 msec per step in the case of a full rotation of 1 sec). In order to collect the Dose, the TLE actor (Track Length Estimator) was used allowing fast dose computation. With the TLE method, photons deposit their energy in a continuous manner all along their trajectory, instead of doing so at discrete interaction points, a fact that substantially reduces the variance [89]. For the same uncertainty, the TLE method required about 50 times less primaries than analogous MC simulation.

2.3. Validation

To validate our results, simulations were performed using single

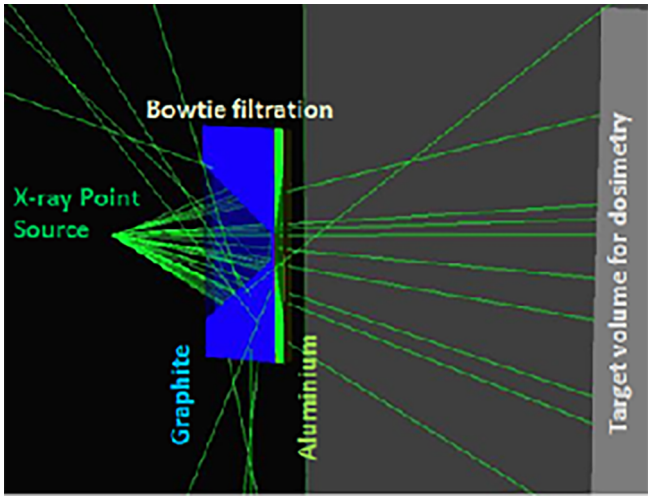

Fig. 1. Visualization of the X-ray point source and the bowtie filter in GATE. Blue color represents the Graphite wedge and green color represents the Aluminum wedge. (For interpretation of the references to color in this figure legend, the reader is referred to the web version of this article.)

axial scan in air and with the 16-cm-diameter PMMA (polymethylmethacrylate) phantom which is used to represent the child's body [15]. The phantom meets the 21 CFR 1020.33 specifications as defined by FDA.[1]

The thin-walled pencil-beam ionization chamber was a Radcal 10 × 5–3CT model and it was simulated according to the manufacturer specifications.

First, we simulated the ionization chamber in air at isocenter and we compared the results with the physical measurements in order to derive the normalization factor in units of particles/mAs [90] for 120 kVp for a nominal beam collimation of 10 mm and 260 mAs:

$$NF_{E,NT} = \frac{(D_{air,\ measured,\ per\ \ mAs})_{E,NT}}{(D_{air,\ simulated\ \ per\ \ mAs})_{E,NT}} \quad (2)$$

where $D_{air,measured\ per\ mAs}$ is the measured air kerma at the scanner isocenter in units of mGy/mAs and $D_{air,simulated\ per\ mAs}$ is the simulated air kerma at the scanner isocenter in units of mGy/particle for the certain beam energy E and beam collimation NT.

The simulated absorbed dose in PMMA head voxelized phantom was compared with physically measured data in corresponding PMMA physical phantoms at one (1) position (at center) and four (4) peripheral positions for 120 kVp, 260 mAs, scan range 10 mm, slice thickness 1 mm and the small bowtie filter. The PMMA cylinder contains three other inner cylinders with plastic (buildup cup), graphite and air respectively. The voxelized CTDI phantom had 160 × 160 × 150 voxels and resolution 1 mm voxel. The output of the simulation was a 3D dose-map, where the absorbed dose (in Grays – Gy) was stored in each voxel of the phantom.

2.4. Anthropomorphic models

This study employed 12 realistic anthropomorphic computational phantoms for the modeling of the pediatric anatomy. One of them was an in-house model and the organs were manually segmented with the 3D Slicer (https://www.slicer.org/) (Fig. 2).

11 more realistic anthropomorphic computational phantoms were employed from DUKE University [91,92] and ITIS foundation databases [93]. DUKE University has developed a series of realistic 4D anthropomorphic models (XCAT model) based on the non-uniform rational b-spline (NURBS) and subdivision (SD) surfaces. The ITIS foundation developed the "Virtual Family"; a series of surface-based anatomical models including 2 children. 2 years later they extended their dataset with a "Virtual Classroom", including 4 more children based on healthy clinical MR data.

Table 1 lists the details of the pediatric models. The lung height was measured from the top to the bottom of the organs. AP and LAT dimensions were also measured for each phantom. The square root of the product of the AP and lateral diameters was then used to calculate the effective diameters [16]. Table A1 in the Appendix reports the masses of the organs of interest for the 12 phantoms that were considered for dosimetry.

2.5. CT examination simulations

The scan ranges for the three helical CT examinations (chest, abdomen/pelvis and head) were obtained from the updated CT scan protocols which are proposed by the Alliance for Quality Computed Tomography (AQCT) for the specific scanner [94].

2.6. Organ dose estimation method

Organ dose estimations were performed by simulating the three typical helical protocols presented in Table 2 for the twelve pediatric male and female computational phantoms. The small bowtie filter was used for every pediatric phantom irradiation. The $CTDI_{vol}$ and the corresponding DLP value were calculated. For each voxelized model, the number of rotations per simulation was calculated based on the length of the irradiated volume, beam collimation and pitch. All the simulations were assumed to start at the 12 "o" clock tube location and 10^8 primaries were used in order to keep statistical uncertainties lower than 2% for organs fully inside the scan range coverage. For very small organs or for organs located at large distances from the primary beam, the statistical uncertainties were kept lower than 5%.

The output of the MC simulations was the deposited energy in units of MeV. The absolute absorbed dose (mGy) per source particle was calculated for each organ and then the absolute dose in mGy was obtained. Eq. (3) was used to obtain the absolute dose from the simulated data:

$$(D_{absolute})_{E,NT} = (D_{simulated\ \ per\ \ 100\ \ mAs})_{E,NT} * (NF)_{E,NT} * \frac{mAs}{rotation} * N \quad (3)$$

where NF is the normalization factor of the corresponding collimation for each protocol, $mAs/rotation$ is the mean clinical tube current (mA) multiplied by the exposure time (s) and N is the number of rotations during this CT scan.

First, contributions to effective dose (mSv/100 mAs) and absorbed doses per $CTDI_{vol}$ (unitless) were presented into tables for all the organs inside and outside scan range. The latest were provided to eliminate scanner-specific characteristics, providing to users the ability to estimate organ doses for any other CT scanner [95]. Variations in organ absorbed dose across the patients were quantified by the coefficient of variation (SD × 100%/mean) for organs both inside and outside the scan coverage.

Absorbed doses per $CTDI_{vol}$ (unitless) were correlated with patient model weight for the organs inside the scan range using exponential regression analysis for chest and abdomen/pelvis protocols. The following equation was used for the dose analysis:

$$Dose\ per\ \ CTDI_{vol} = \exp(a \times \ \ total\_weight + b) \quad (4)$$

where *Dose per $CTDI_{vol}$ and total weight* are unitless and in the units of kg, respectively. The regression fit coefficients were calculated with an in-house script generated in Python.

Finally, *Effective Doses per DLP* in units of μSv/(mGy*cm) were calculated as a function of total weight for the twelve phantoms. *Effective Doses per DLP* is also a way to eliminate the dependence on the scanner model [27]. The following equation was used:

$$Effective\ \ Dose\ \ per\ \ DLP = exp(a \times total\_weight + b) \quad (5)$$

[1] https://www.accessdata.fda.gov/scripts/cdrh/cfdocs/cfcfr/CFRSearch.cfm?FR=1020.33.

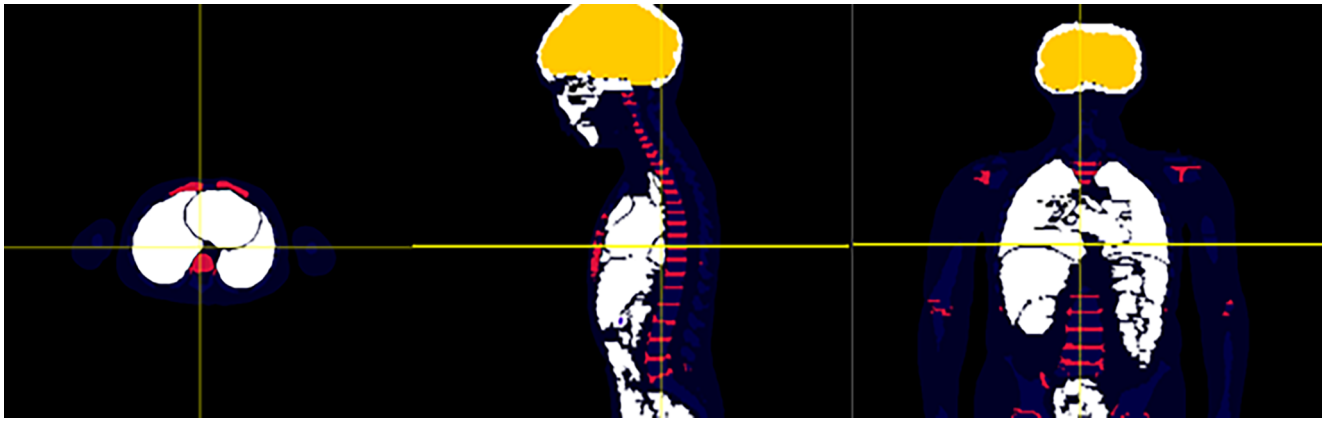

Fig. 2. Orthogonal views of the segmented 5 year-male.

Table 1
Characteristics of the pediatric models' population.

No. (#)	Age (y)	Gender	Type	Weight (Kg)	Height (m)	BMI (kg/m^2)	Lung (cm)	Eff. Diameter (cm)	Size (No. of voxels)	Voxel Size (mm^3)
1	2.1	F	XCAT	12.2	0.86	16.5	6.8	7.2	390 × 336 × 910	1 × 1 × 1
2	2.8	M	XCAT	14.1	0.92	16.7	8	8	448 × 276 × 1004	
3	3.3	F	XCAT	13.8	0.93	16	7.1	7.7	378 × 304 × 1032	
4	3.7	M	XCAT	16.2	0.97	17.2	8.7	8.4	430 × 286 × 1066	
5	5	M	In-house	14.75	1	14.8	16	16.8	512 × 511 × 190	0.9 × 0.9 × 3.2
6	5	F	ITIS	17.7	1.09	14.9	12.6	16.6	350 × 203 × 1102	1 × 1 × 1
7	6	M	ITIS	18.6	1.16	13.8	13.5	17.7	403 × 225 × 1181	
8	8	F	ITIS	29.64	1.36	16.2	15.4	19.2	600 × 243 × 1607	
9	8	M	ITIS	25.6	1.37	13.5	17.3	19	435 × 252 × 2572	
10	11	F	ITIS	34	1.49	15.3	16.1	20.7	500 × 280 × 1560	
11	14	M	ITIS	50.38	1.68	17.6	20.2	26	483 × 312 × 1726	
12	14	F	XCAT	39.8	1.4	20.3	17.4	21	250 × 250 × 690	

Table 2
The CT Protocols used in this study.

Protocol	Chest scan from top of shoulder through mid-liver	Abdomen/pelvis scan from top of liver to pubic symphysis	Head scan from base of skull through vertex
beam collimation (mm)	20	20	20
pitch	1.38	1.38	0.531
table feed (mm/rot)	27.50	27.50	10.62
time (s)/rot	0.4	0.4	0.5
table speed (mm/s)	68.75	68.75	21.24
mAs/rot	30	30	93
kV	100 & 120	100 & 120	100 & 120

Table 3
Measured and simulated $CTDI_{100}$ in air at isocenter and derived normalization factor are reported for 120 kVp for a nominal beam collimation of 10 mm.

Energy (kVp)	Measured $CTDI_{100}$ in air (mGy mAs$^{-1)}$	Simulated $CTDI_{100}$ in air (mGy particle^{-1})	Normalization factor (particle mAs^{-1})
120	3.65×10^{-1}	1.23×10^{-12}	2.96×10^{11}

3. Results

3.1. Model validation and calibration

First, the $CTDI_{100}$ in air was measured from the isocenter for the 120 kVp and 260 mAs by using the ion chamber kVp for a nominal beam collimation of 10 mm. The same experiment was simulated with GATE and the $CTDI_{100}$ in air (in units of mGy particle^{-1}) was estimated in order to derive the normalization factor (Table 3).

Doses for five different positions (central dose and doses at 12, 3, 6 and 9 o'clock positions) were measured within the CTDI head phantom by using the ion chamber with the collimation of 10 mm under the 120 kVp (Table 4).

The statistical uncertainty of the simulated data, in the CDTI dose simulations was less than 2%. In addition, the experimental measurements also provided errors less than 2%. The percentage difference between simulated and corresponding experimental data was up to 11%. This difference may be attributed to the accuracy of the modelled ion chamber in GATE compared to the experimental one. Nevertheless, any model in GATE with geometrical components is ideally designed (in our case, the ion chamber and the description of the source, bowties, etc.) and could even differ in elemental composition to the one that was experimentally used. Such differences are considered acceptable, taking also in account the statistical uncertainties of the simulations [62]. Straton et al. also presented similar differences up to 8.6% from the comparison of simulated $CTDI_{100}$ values compared to the experimentally measured values.

Table 4
Comparison of CTDIw between simulated and clinical data.

Position for head phantom	Ion chamber dose (mGy)	Simulated dose (mGy)	Difference %
Periph. 12 o'clock	48.59	54.37	11.23
Periph. 3 o'clock	48.59	54.39	11.26
Periph. 6 o'clock	48.59	54.77	11.96
Periph. 9 o'clock	48.59	54.73	11.89
center	46.41	51.05	9.52
$CTDI_w$	47.86	53.39	10.92

3.2. Simulation of patient doses

3.2.1. Patient absorbed doses

The normalization factor for the 20 mm beam collimation of the protocols was 1.361×10^{13} and 2.044×10^{11} particles per 100 mAs for 100 and 120 kVp respectively.

Absorbed doses per $CTDI_{vol}$ and per 100 mAs and the corresponding variations in organ doses across the patients are reported for the three protocols. More specific, variations between 23 and 42% and 30–32% (Table A2a, b in the Appendix) were observed across the pediatric population for organs fully inside the chest acquisition for 100 and 120 keV, while much bigger variations (up to 799%) were noticed for organs partially irradiated. Respectively for the two other protocols, the absorbed dose received by fully irradiated organs varied between 23 and 40% and 19–25% in the abdomen (Table A3a, b in the Appendix) and between 12 and 297% and 13–109% for the head scan acquisition (Table A4a, b in the Appendix) for 100 and 120 keV respectively.

Contributions to effective doses (mSv/100 mAs) for all the cases are reported in Tables A5–A7 in the Appendix. Figs. 3 and 4 show absorbed doses per $CTDI_{vol}$ (unitless) correlated with patient model weight for indicative organs inside the scan range using exponential regression analysis for chest and abdomen/pelvis protocols.

The position and the mass of each organ determine the dependency magnitude. The association was strong for some organs inside the scan coverage; the coefficient of determination (R^2) was between 0.5 and 0.6 for all organs inside the scan range for the chest protocol, and between 0.5 and 0.7 for liver, kidneys, gallbladder, spleen, pancreas and large intestine for the abdomen/pelvis protocol (Table 5).

3.2.2. Effective doses per DLP

Effective doses per DLP in μSv/(mGy*cm) were gathered for all the scan protocols as a function of total weight for 100 and 120 keV (Fig. 5).

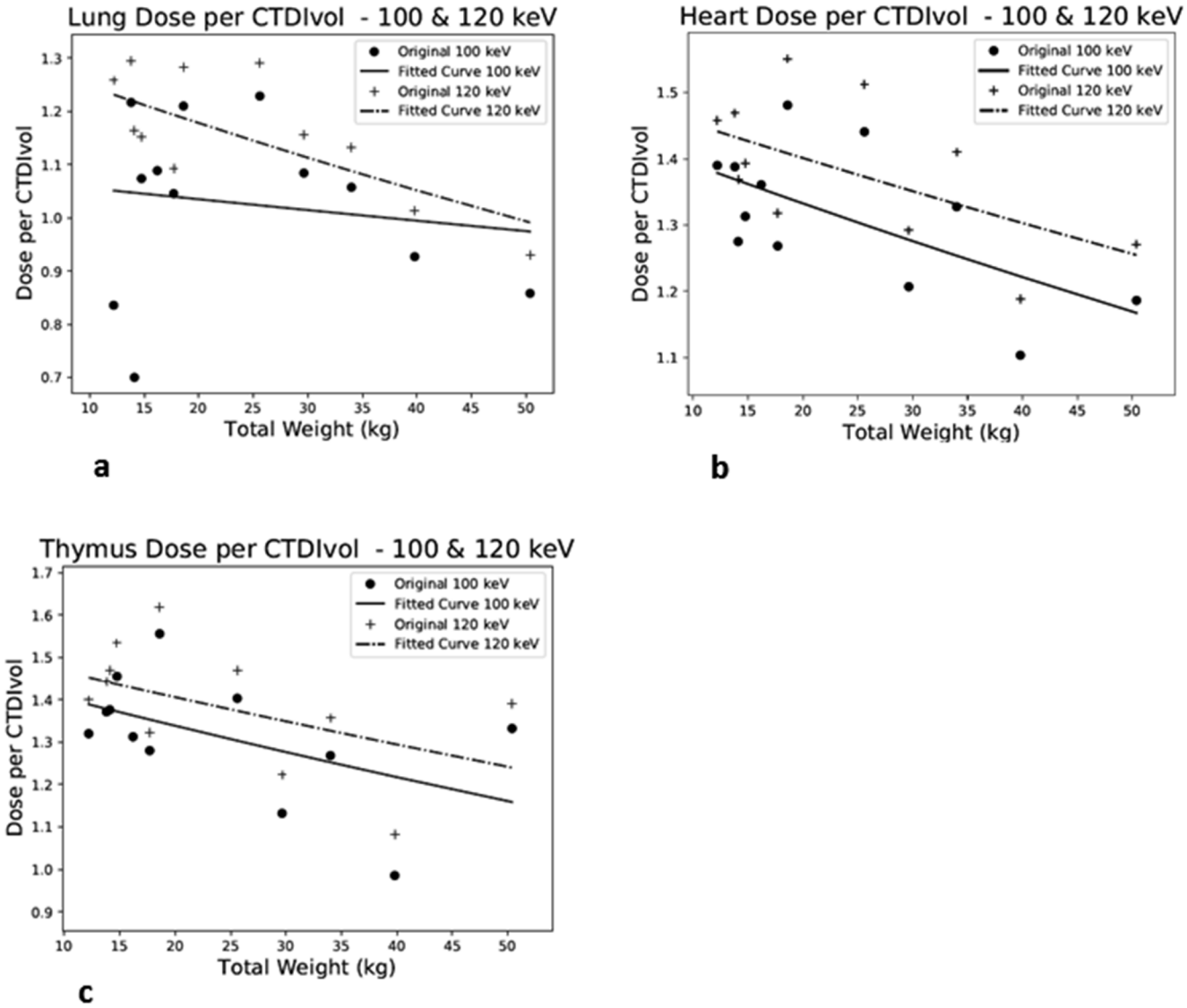

Fig. 3. Absorbed doses per $CTDI_{vol}$ (unitless) in the chest MDCT scan, correlated with patient model weight using exponential regression analysis for organs inside the scan range for 100 and 120 keV; a. Lung, b. Heart, and c. Thymus.

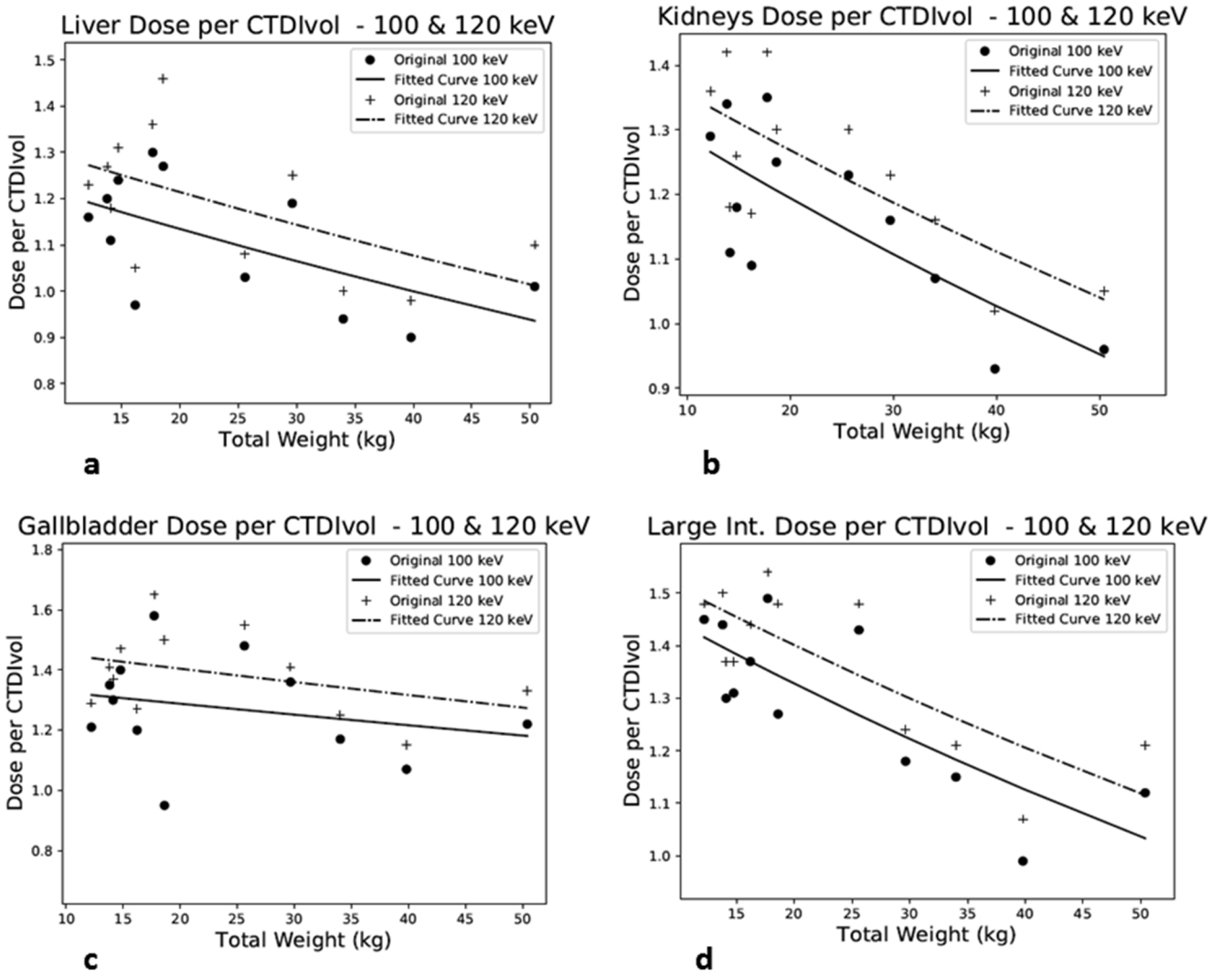

Fig. 4. Absorbed doses per $CTDI_{vol}$ (unitless) in the abdomen MDCT scan, correlated with patient model weight using exponential regression analysis for indicative organs inside the scan range for 100 and 120 keV; a. Liver, b. Kidneys, c. Gallbladder, and d. Large Intestine.

Table 5
Regression fit coefficient for absorbed doses per $CTDI_{vol}$ as a function of total weight for chest and abdomen protocol (100 keV and 120 keV).

Fully internal scan – organs	a*	b*	R^{2**}	a*	b*	R^{2**}
	100 keV			120 keV		
CHEST						
lung	−0.002	0.074	0.5	−0.005	0.277	0.5
heart	−0.004	0.374	0.6	−0.003	0.41	0.5
thymus	−0.005	0.387	0.6	−0.004	0.424	0.6
ABDOMEN						
liver	−0.007	0.253	0.5	−0.006	0.314	0.5
kidneys	−0.007	0.328	0.6	−0.006	0.369	0.6
gallbladder	−0.003	0.31	0.6	−0.003	0.404	0.7
large intestine	−0.008	0.449	0.7	−0.007	0.487	0.7

*a and b are fit coefficients for the equation relating absorbed doses per $CTDI_{vol}$ to total weight.
**R^2 is the coefficient determination for the fit.

A good correlation between dose and total weight is suggested by high R^2-coefficents ($R^2 > 0.8$) (Table 6) for chest and abdomen protocol but a very small correlation was arised for the head protocol.

The current values of *effective doses per DLP* were compared with the corresponding values generated by Lee C et al. [48] (Table 7). These values are based on ICRP 103 pediatric reference phantoms which were developed at the University of Florida and the National Cancer Institute. The differences were comparable with the corresponding differences given in other studies (up to 33% from the comparison between Lee et al. and Shrimpton et al. [32,48]) and can be explained due to anatomical differences in the phantoms and the different scanned regions.

4. Discussion

The GATE MC toolkit is well validated for dosimetry and widely used by scientific community. We have already used it for internal sources of radiation [96]; its use for simulating external dosimetry applications has been already demonstrated [97].

In this study, we reported patient-specific radiation dose from pediatric chest, abdomen/pelvis and head CT examinations using twelve pediatric male and female patients. Simulating different pediatric patients in the same size/protocol group, we acquired the assessment of dose variations across the patients due to the variability of patient anatomy and body size, which could not be obtained using previous methods of DLP. The patient-specific computational phantoms are considered to be the best representation in terms of physiological and functional information of the human body at the organ and cellular levels.

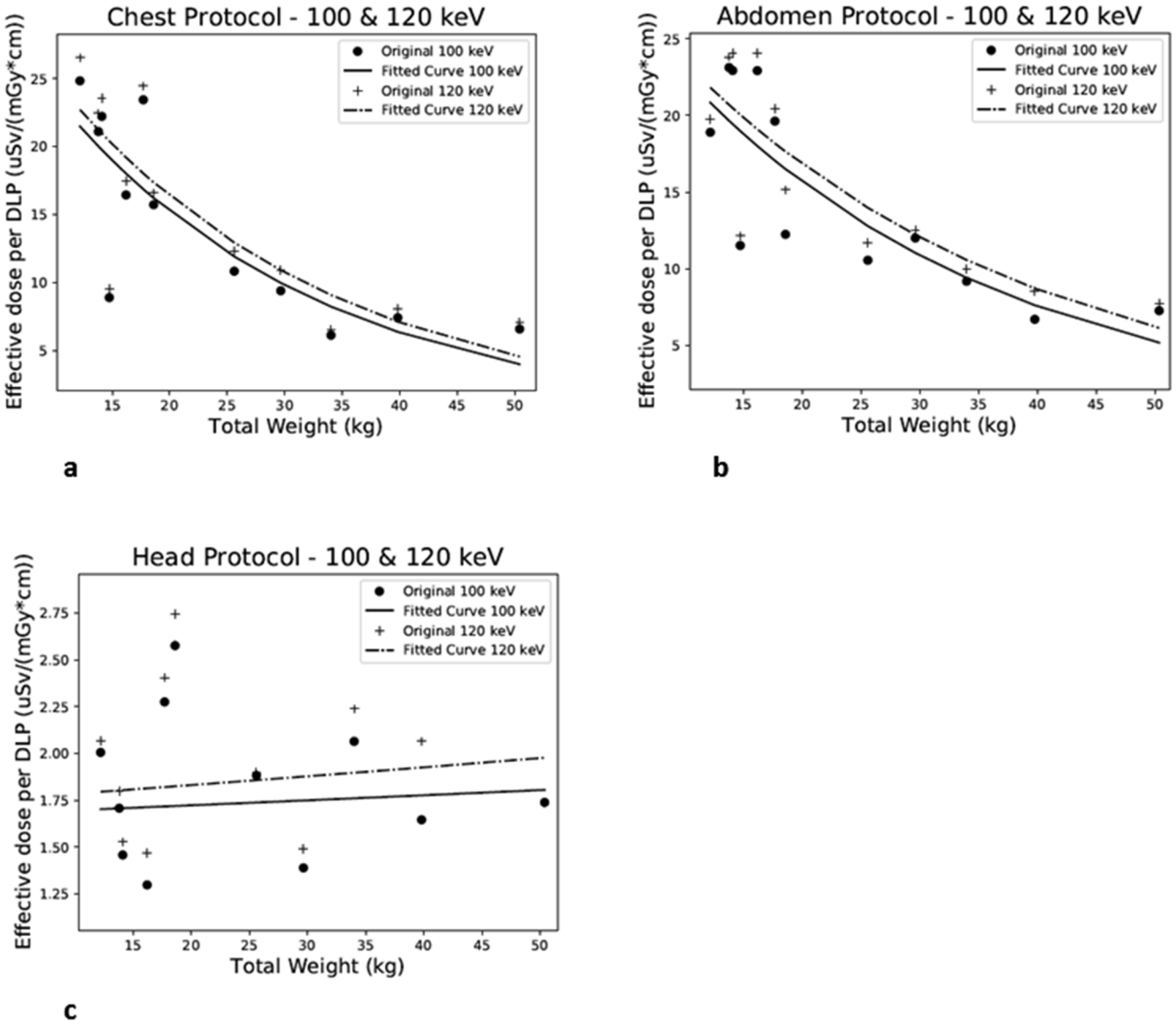

Fig. 5. Comparison of effective doses per DLP (μSv/(mGy*cm)) for the different pediatric phantoms for 100 and 120 keV; a. chest, b. abdomen, and c. head scan.

Table 6
Regression fit coefficient for effective doses per DLP as a function of weight (100 keV and 120 keV).

Protocol	a*	b*	R^{2}**	a*	b*	R^{2}**
	100 keV			120 keV		
chest	−0.044	3.603	0.9	−0.042	3.635	0.9
abdomen	−0.036	3.481	0.8	−0.033	3.488	0.8
head	0.002	0.513	0.2	0.003	0.554	0.1

*a and b are fit coefficients for the equation relating effective doses per DLP to total weight.
**R^2 is the coefficient determination for the fit.

The simulated CTDI values were in good agreement with the measured that were provided by the manufacturer. The observed discrepancies (up to 11%) may be attributed to uncertainties in modelling the scanner, even though they follow closely previous work. Similar differences are published in literature [69].

Secondly, absorbed doses per $CTDI_{vol}$ were correlated with patient model weight for the organs inside the scan range using exponential regression analysis for chest and abdomen/pelvis protocols.

Anatomical differences, in children of similar age and/or weight, resulted in calculated absorbed dose differences up to 40% in organs within the scan range of the chest protocol. Exceptions were recorded in thymus and heart in the 3 y male and female phantoms where dose differences were 49.50% and 51% respectively. The corresponding organ's mass differences reached 31.55% and 30% respectively, whereas the total body's mass difference of the 3 y male and female was 16%. In addition, 62% difference was calculated in heart's absorbed dose between the 5 y in-house male (14.75 kg total body mass) and the 5 y ITIS phantom (17.7 kg total body mass). Calculated dose differences up to 28% were observed in organs within the scan range of the abdomen protocol. Exceptions were recorded in the calculated absorbed dose to the gallbladder, kidneys and large intestine in the 6 y male (18.6 kg total body mass) and the 5 y female (14.75 kg total body mass). For these organs, we observed absorbed dose differences up to 56.05%, 64.60%, and 56.27% with the corresponding organs' mass differences reaching 19.86%, 25% and 123.86% respectively. In the head protocol, anatomical differences in children of similar age and/or weight resulted in organ dose differences up to 30%, except skull's absorbed dose in the 14 y male and female XCAT phantoms which reached 124.15% difference. The total head's mass difference reached 151.23%, while the

Table 7
Comparison of the factors generated by Lee et al. [48] and the current study. The percent difference was calculated as (reference value-this study)/reference value.

Phantom	Effective Dose/DLP (mSv/(mGy*cm))					
	100 kVp			120 kVp		
	Lee et al.	Present study	*Difference %*	Lee et al.	Present study	*Difference %*
Chest						
5-year-old	0.023	0.023	*3.247*	0.024	0.024	*1.832*
10-year-old	0.016	0.015	*5.349*	0.017	0.012	*26.832*
15-year-old	0.011	0.007	*32.44*	0.012	0.007	*41.211*
Abdomen						
5-year-old	0.021	0.02	*5.206*	0.022	0.02	*7.525*
10-year-old	0.013	0.011	*18.2*	0.017	0.011	*30.338*
15-year-old	0.01	0.007	*29.474*	0.014	0.007	*32.099*
Head						
5-year-old	0.004	0.002	*40.126*	0.004	0.0024	*44.078*
10-year-old	0.003	0.002	*20.625*	0.003	0.0019	*34.537*
15-year-old	0.002	0.002	*8.506*	0.002	0.0021	*4.545*

skull's mass difference was 161.15% for the two models.

Finally, effective doses per DLP were estimated for each case. These factors are different from the existing reference values and this can be explained by anatomical differences in the phantoms and scanned regions used. Our basic goal was to define the dependence of the effective doses per DLP on body and organ mass and not to replace the existing reference values. Higher effective doses effective doses per DLP do not necessarily mean higher effective doses, as the DLP has to be kept appropriately low in pediatric CT practice, which reduces the effective dose and offsets the effects of higher conversion factors. A good correlation between dose and total weight is suggested in the current study ($R^2 > 0.8$) (Table 6) for the chest and abdomen protocols. The results for the head protocol indicated a very poor correlation between dose and the patient's weight. This was due to the fact that head weights of the patient-specific phantoms were not proportionate to the total mass of the total phantom weight.

Compared with the values obtained by Lee et al., our computed effective doses effective doses per DLP for the peadiatric models had average discrepancies, for 100 keV, 13%, 17% and 23% for chest, abdomen/pelvis and head protocols respectively. For 120 keV the corresponding average discrepancies were 23% for the chest and abdomen/pelvis and 27% for the head protocols. The discrepancies of these values are comparable to published literature [32,48] and are mainly attributed to anatomical differences present in the phantoms, as well as the different scanned regions. Indicatively, up to 33% organ dose differences were presented in the chest protocol of Lee et al. compared to the study of Shrimpton et al. [48].

Across the different kind of phantoms, the internal organs vary in number and in morphology, such as shape, dimensions and position. In addition, the relative position of the organs in the scan coverage is different in every case and the same scan region is hard to be defined.

5. Conclusions

As reported in the results and discussion section absorbed dose per organ, in pediatric CT protocols plays a crucial role, and high variations are reported, due to anatomical differences. In this study GATE MC Simulation toolkit was used incorporating a population of different pediatric models in order to estimate such differences. Based on such reported results, the idea is to extend the CT dosimetry database, by using a large population of pediatric models, and to improve the accuracy of external dosimetry for new patients undergoing CT exams. Providing such dosimetry datasets for each pediatric protocol (including pediatric models with differences in anatomy), the clinician should be able to assess internal absorbed doses per organ before the CT acquisition. The individualized anatomical characteristics will be considered to match each patient to the closest model of the existed database.

Our aim is to use this database for future patients, estimating the absorbed dose by correlating the patient to one of the database's phantoms. More precisely, more phantoms should be included in the database, and with the aid of Machine Learning techniques, be able to estimate the absorbed dose per organ, taking into account several anatomical characteristics of the patient. Indicatively, the lung height could thus be used as an additional internal anatomy parameter, should the CT of the new patient is available. The lung is one of the easiest organs to segment, and its height can be automatically extracted and used for the best matching of the patient to the closest available phantom.

Acknowledgements

This study was funded by the European Union's Horizon 2020 Research and Innovation Programme under the Marie Skłodowska-Curie grant agreement No 691203. The results published in this study reflect only the author's view and the Research Executive Agency (REA) and the European Commission is not responsible for any use that may be made of the information it contains. This work was supported by computational time granted from the Greek Research & Technology Network (GRNET) in the National HPC facility — ARIS — under project ID pi170404-MC:CANCEL. Thanks to the Greek State Scholarship Foundation, "Human Resources Development, Education and lifelong learning" (NSRF 2014-2020). An action entitled "Scholarship Scheme for postgraduate studies in second cycle" and code ΟΠΣ5003404. The authors would also like to thank GE for providing technical parameters of the GE BrightSpeed Elite 16 Slice CT scanner and PhD Candidate Konstantinos Chatzipapas for his direct technical support in modeling and analysis issues.

Appendix A. Supplementary data

Supplementary data to this article can be found online at https://doi.org/10.1016/j.ejmp.2019.08.020.

References

[1] Dauer L, Hricak H. Addressing the challenge of managing radiation use in medical imaging: paradigm shifts and strategic priorities. Oncology-Ny 2014;28:243–4.
[2] ICRP. Managing patient dose in multi-detector computed tomography (MDCT). ICRP Publication 102. Ann ICRP 2007;37:1–80.
[3] ICRP. Managing patient dose in computed tomography. Ann ICRP 2000;2000(30):1–86.
[4] Schauer D, Linton O. NCRP Report No. 160, ionizing radiation exposure of the

population of the United States, medical exposure-are we doing less with more, and is there a role for health physicists? Health Phys 2009;97(1):1–5.
[5] UNSCEAR. Sources and effects of ionizing radiation. United Nations scientific committee on the effects of atomic radiation 2008 report. 2008. p. 2.
[6] WHO. Communicating radiation risks in paediatric imaging: information to support health care discussions about benefit and risk. World Health Organization; 2016.
[7] Robbins E. Radiation risks from imaging studies in children with cancer. Pediatr Blood Cancer 2008;51:453–7.
[8] UNSCEAR. Sources, Effects and risks of ionizing radiation. United Nations scientific committee on the effects of atomic radiation. 2013.
[9] Pearce M, Salotti J, Little M, McHugh K, Lee C, Kim K, et al. Radiation exposure from CT scans in childhood and subsequent risk of leukaemia and brain tumours: a retrospective cohort study. Lancet 2012;380:499–505.
[10] Brenner D, Doll R, Goodhead D, Hall E, Land C, Little J, et al. Cancer risks attributable to low doses of ionizing radiation: assessing what we really know. Proc Natl Acad Sci USA 2003;100:13761–5.
[11] Frush D, Donnelly L, Rosen N. Computed tomography and radiation risks: what pediatric health care providers should know. Pediatrics 2003;112:951–7.
[12] Belley MD, Wang C, Nguyen G, Gunasingha R, Chao NJ, Chen BJ, et al. Toward an organ based dose prescription method for the improved accuracy of murine dose in orthovoltage x-ray irradiators. Med Phys 2014;41:034101–34107.
[13] Brenner D, Elliston C, Hall E, Berdon W. Estimated risks of radiation-induced fatal cancer from pediatric CT. AJR Am J Roentgenol 2001;176:289–96.
[14] Brenner D, Hall E. Cancer risks from CT scans: now we have data, what next? Radiology 2012;265:330–1.
[15] AAPM. The Measurement, Reporting, and Management of Radiation Dose in CT. AAPM REPORT NO. 96. Report of AAPM Task Group 232008. pp. 1–28.
[16] AAPM. Size-Specific Dose Estimates (SSDE) in Pediatric and Adult Body CT Examinations. AAPM Report No. 204. Report of AAPM Task Group 204; 2011.
[17] AAPM. Use of Water Equivalent Diameter for Calculating Patient Size and Size-Specific Dose Estimates (SSDE) in CT. AAPM REPORT NO. 220. The Report of AAPM Task Group 220; 2014.
[18] Moore B, Brady S, Mirro A, Kaufman R. Size-specific dose estimate (SSDE) provides a simple method to calculate organ dose for pediatric CT examinations. Med Phys 2014;41:07191–7201.
[19] Schmidt B, Saltybaeva N, Kolditz D, Kalender W. Assessment of patient dose from CT localizer radiographs. Med Phys 2013;40:084301–84308.
[20] Boos J, Meineke A, Bethge O, Antoch G, Kröpil P. Dose monitoring in radiology departments: status quo and future perspectives. Rofo 2016;188:443–7.
[21] Heilmaier C, Zuber N, Bruijns B, Ceyrolle C, Weishaupt D. Implementation of dose monitoring software in the clinical routine: first experiences. Fortschr Röntgenstr 2016;188:82–8.
[22] Shrimpton P, Hillier M, Lewis M, Dunn M. Doses from computed tomography (CT) examinations in the UK-2003 review. In: (NRPB) NRPB, editor. Chilton, UK NRPB-W67 ed.; 2005.
[23] Kanal K, Butler P, Sengupta D, Bhargavan-Chatfield M, Coombs L, Morin RUS. Diagnostic reference levels and achievable doses for 10 adult CT examinations. Radiology 2017;284:120–33.
[24] Cristy M, Eckerman K. Specific Absorbed Fractions of Energy at Various Ages from Internal Photon Sources. Oak Ridge National Laboratory. United States: ORNL/TM-8381/V1-V7; 1987.
[25] Shrimpton P, Jessen K, Geleijns J, Panzer W, Tosi G. Reference doses in computed tomography. Rad Prot Dosim 1998;80:55–9.
[26] Menzel H, Schibilla H, Teunen D. European guidelines on quality criteria for computed tomography. European Commission; 2000.
[27] Huda W, Ogden K, Khorasani M. Converting dose-length product to effective dose at CT. Radiology 2008;248:995–1003.
[28] Shrimpton P, Wall B. Reference doses for paediatric computed tomography. Radiat Prot Dosim 2000;90:249–52.
[29] Commission E. European guidelines on quality criteria for computed tomography. In: 2004, editor.: European Commission Report EUR 16262; 2004.
[30] Deak P, Smal Y, Kalender W. Multisection CT protocols: sex- and age-specific conversion factors used to determine effective dose from dose-length product. Radiology 2010;257:158–66.
[31] Adult ICRP. Reference computational phantoms. ICRP publication 110. Ann ICRP 2009;39.
[32] Romanyukha A, Folio L, Lamart S, Simon S, Lee C. Body size-specific effective dose conversion coefficients forct scans. Radiat Prot Dosimetry 2016;172:428–37.
[33] Chapple C, Willis S, Frame J. Effective dose in paediatric computed tomography. Phys Med Biol 2002;47:107–8.
[34] Fujii K, Aoyama T, Koyama S, Kawaura C. Comparative evaluation of organ and effective doses for paediatric patients with those for adults in chest and abdominal CT examinations. Br J Radiol 2007;80:657–67.
[35] Zhang D, Li X, Gao Y, Xu X, Liu B. A method to acquire CT organ dose map using OSL dosimeters and ATOM anthropomorphic phantoms. Med Phys 2013;40:081918–81919.
[36] DeMarco J, Cagnon C, Cody D, Stevens D, McCollough C, O'Daniel J, et al. A Monte Carlo based method to estimate radiation dose from multidetector CT (MDCT): cylindrical and anthropomorphic phantoms. Phys Med Biol 2005;50:3989–4004.
[37] Caon. Voxel-based computational models of real human anatomy: a review. Radiat Environ Biophys 2004;42:229–36.
[38] Geleijns J, Joemai R, Cros M, Hernandez-Giron I, Calzado A, Dewey M, et al. A Monte Carlo simulation for the estimation of patient dose in rest and stress cardiac computed tomography with a 320-detector row CT scanner. Phys Med 2015;31:1029–34.
[39] Kalender W, Saltybaeva N, Kolditz D, Hupfer M, Beister M, Schmidt B. Generating and using patient-specific whole-body models for organ dose estimates in CT with increased accuracy: feasibility and validation. Phys Med 2014;30:925–33.
[40] Turner A, Zhang D, Kim H, DeMarco J, Cagnon C, Angel E, et al. A method to generate equivalent energy spectra and filtration models based on measurement for multidetector CT Monte Carlo dosimetry simulations. Med Phys 2009;36:2154–64.
[41] Turner A, Zhang D, Khatonabadi M, Zankl M, DeMarco J, Cagnon C, et al. The feasibility of patient size-corrected, scanner-independent organ dose estimates for abdominal CT exams. Med Phys 2011;38:820–9.
[42] http://www.impactscan.org/ctdosimetry.htm.
[43] Heron L. CTDOSE: a user's guide. Software and manual New Zealand, National Radiation Laboratory; 1993.
[44] Radimetrics. eXposure 2012, 2012.
[45] Kalender W, Schmidt B, Zankl M, Schmidt M. A PC program for estimating organ dose and effective dose values in computed tomography. Eur Radiol 1999;9:555–62.
[46] Zankl M, Panzer W, Drexler G. The Calculation of Dose from External Photon Exposures Using Reference Human Phantoms and Monte Carlo Methods, Part VI: Organ Doses From Computed Tomographic Examinations. Munchen: GSF-Gesellschaft fur Strahlen und Umweltforschung mbH1991. p. 1–195.
[47] Kramer R, Zankl M, Williams G, Drexler G. The Calculation of Dose from External Photon Exposures Using Reference Human Phantoms and Monte-Carlo Methods, Part 1: The Male (ADAM) and Female (EVA) Adult Mathematical Phantoms; 1982.
[48] Lee C, Kim K, Long D, Bolch W. Organ doses for reference pediatric and adolescent patients undergoing computed tomography estimated by Monte Carlo simulation. Med Phys 2012;39:2129–46.
[49] Stamm G, Nagel H. CT-expo-a novel program for dose evaluation in CT. Fortschr Röntgenstr 2002;174:1570–6.
[50] Zankl M, Panzer W, Petoussi-Henss H, Drexler G. Organ doses for children from computed tomographic examinations radiation protection dosimetry. Radiat Prot Dosimetry 1995;57:393–6.
[51] Veit R, Zankl M, Petoussi N, Mannweiler E, Drexler D. Tomographic anthropomorphic models: part I. In: 3/89 G-BR3/89 G-BReditor. Construction technique and description of models of an 8 week old baby and a 7 year old child. Neuherberg, Germany: National Research Center for Environment and Health; 1989.
[52] Ban N, Takahashi F, Sato K, Endo A, Ono K, Hasegawa T, et al. Development of a web-based CT dose calculator: WAZA-ARI. Radiat Prot Dosim 2011:333–7.
[53] CT_Imaging. ImpactDose.
[54] Lee C, Kim K, Bolch W, Moroz B, Folio L. NCICT: a computational solution to estimate organ doses for pediatric and adult patients undergoing CT scans. J Radiol Prot 2015;35:891–909.
[55] Xu X. An exponential growth of computational phantom research in radiation protection, imaging, and radiotherapy: a review of the fifty-year history. Phys Med Biol 2014;59:233–302.
[56] Zaidi H, Xu X. Computational anthropomorphic models of the human anatomy: the path to realistic Monte Carlo modeling in radiological. Annu Rev Biomed Eng 2007;9:471–500.
[57] Na Y, Zhang B, Zhang J, Caracappa P, Xu X. Deformable adult human phantoms for radiation protection dosimetry: anthropometric data representing size distributions of adult worker populations and software algorithms. Phys Med Biol 2010;55:3789–811.
[58] Lee C, Lodwick D, Hurtado J, Pafundi D, Williams J, Bolch W. The UF family of reference hybrid phantoms for computational radiation dosimetry. Phys Med Biol 2010;55:339–63.
[59] Lee C, Lodwick D, Williams J, Bolch W. Hybrid computational phantoms of the 15-year male and female adolescent: applications to CT organ dosimetry for patients of variable morphometry. Med Phys 2008;35:2366–82.
[60] Ding A, Gao Y, Liu H, Caracappa P, Long D, Bolch W, et al. VirtualDose: a software for reporting organ doses from CT for adult and pediatric patients. Phys Med Biol 2015;60:5601–25.
[61] Gao Y, Quinn B, Pandit-Taskar N, Behr G. Patient-specific organ and effective dose estimates in pediatric oncology computed tomography. Phys. Med 2018;45:146–55.
[62] Straton R, Lee C, Lee C, Williams M, Hintenlang D, Arreola M, et al. Organ and effective doses in newborn patients during helical multislice computed tomography examination. Phys Med Biol 2006;51:5151–66.
[63] Lee C, Lee C, Staton RJ, Hintenlang DE, Arreola MM, Williams JL, et al. Organ and effective doses in pediatric patients undergoing helical multislice computed tomography examination. Radiat Protect Phys 2007;34:1858–73.
[64] Li X, Samei E, Segars W, Sturgeon G, Colsher J, Frush D. Patient-specific radiation dose and cancer risk for pediatric chest CT. Radiology 2011;259:862–74.
[65] Tian X, Li X, Segars W, Paulson E, Frush D, Samei E. Pediatric chest and abdominopelvic CT: organ dose estimation based on 42 patient models. Radiology 2014;270:535–47.
[66] Papadakis A, Perisinakis K, Damilakis J. Development of a method to estimate organ doses for pediatric CT examinations. Med Phys 2016;43:2108–18.
[67] Gao Y, Quinn B, Mahmood U, Long D, Erdi D, Germain J, et al. A comparison of pediatric and adult CT organ dose estimation methods. BMC Med Imaging 2017;17–28.
[68] Schlattl H, Zankl M, Becker J, Hoeschen C. Dose conversion coefficients for paediatric CT examinations with automatic tube current modulation. Phys Med Biol 2012;57:6309–26.
[69] Gu J, Bednarz B, Caracappa P, Xu X. The development, validation and application of a multi-detector CT (MDCT) scanner model for assessing organ doses to the pregnant patient and the fetus using Monte Carlo simulations. Phys Med Biol 2009;54:2699–717.
[70] Muryn J, Morgan A, Liptak C, Dong F, Segars W, Primak A, et al. Analysis of uncertainties in Monte Carlo simulated organ and effective dose in chest CT: scanner-

and scan-related factors. Phys Med Biol 2017;62:3175–203.
[71] Kost S, Fraser N, Carver D, Pickens D, Price R, Hernanz-Schulman M, et al. Patient-specific dose calculations for pediatric CT of the chest, abdomen and pelvis. Pediatr Radiol 2015;45:1771–80.
[72] Carver D, Kost SD, Fraser ND, Segars WP, Pickens DR, Price RR, et al. Realistic phantoms to characterize dosimetry in pediatric CT. Pediatr Radiol 2017;47:691–700.
[73] Papadimitroulas P, Kostou T, Chatzipapas C, Visvikis D, Mountris AK, Jaouen V, et al. A review on personalized pediatric dosimetry applications using advanced computational tools. IEEE Trans Radiat Plasma Med Sci 2018.
[74] Kainz Wolfgang, Neufeld Esra, Bolch Wesley E, Graff Christian G, Kim Chan Hyeong, Kuster Niels, et al. Advances in computational human phantoms and their applications in biomedical engineering—a topical review. IEEE Trans Radiat Plasma Med Sci 2018.
[75] Perisinakis K, Pouli S, Tzedakis A, Spanakis A, Hatzidakis A, Raissaki M, et al. What is the underestimation of radiation dose to the pediatric thyroid gland from contrast enhanced CT, if contrast medium uptake is not taken into account? 2018. Phys Med 2018;49:95–8.
[76] Marshall EL, Borrego D, Tran T, Fudge JC, Bolch WE. Evaluation of the UF/NCI hybrid computational phantoms for use in organ dosimetry of pediatric patients undergoing fluoroscopically guided cardiac procedures. Phys Med Biol 2018;63:055006–55022.
[77] Stepusin EJ, Long DJ, Marshall EL, Bolch WE. Assessment of different patient-to-phantom matching criteria applied in Monte Carlo-based computed tomography dosimetry. Med Phys 2017;44:5498–508.
[78] Jan S, Santin G, Strul D, Staelens S, Assié K, Autret D, et al. GATE: a simulation toolkit for PET and SPECT. Phys Med Biol 2004;49:4543–61.
[79] Sarrut D, Bardiès M, Boussion N, Freud N, Jan S, Létang J, et al. A review of the use and potential of the GATE Monte Carlo simulation code for radiation therapy and dosimetry applications. Med Phys 2014;41:064301–64314.
[80] Fedon C, Longo F, Mettivier G, Longo R. GEANT4 for breast dosimetry: parameters optimization study. Phys Med Biol 2015;60:311–23.
[81] Smekens F, Letang JM, Noblet C, Chiavassa S, Delpon G, Freud N, et al. Split exponential track length estimator for Monte-Carlo simulations of small-animal radiation therapy. Phys Med Biol 2014;59:7703–15.
[82] Papadimitroulas P. Dosimetry applications in GATE Monte Carlo toolkit. Phys Med 2017;41:136–40.
[83] Allison J, et al. Geant4 developments and applications. IEEE Trans Nucl Sci 2006;53:270–8.
[84] Agostinelli S, et al. Geant4 – a simulation toolkit. Nucl Instrum Meth Phys Res 2003;A506:250–303.
[85] Allison J, et al. Recent developments in Geant4. Nucl Instrum Meth 2016;A835:186–225.
[86] Siewerdsen J, Waese A, Moseley D, Richard S, Jaffray D. Spektr: a computational tool for x-ray spectral analysis and imaging system optimization. Med Phys 2004;31:3057–67.
[87] Boone J, Seibert J. An accurate method for computer-generating tungsten anode x-ray spectra from 30 to 140 kV. Med Phys 1997;24:1661–70.
[88] Fewell T, Shuping R, Ke H. Handbook of computed tomography X-ray spectra 81-8162 (U.S. Government Printing Office, Washington, D.C.). HHS Publication (FDA); 1981.
[89] Baldacci F, Mittone A, Bravin A, Coan P, Delaire F, Ferrero C, et al. A track length estimator method for dose calculations in low-energy X-ray irradiations: implementation, properties and performance. Med Phys 2015;25:36–47.
[90] Jarry G, DeMarco J, Beifuss U, Cagnon C, McNitt-Gray M. A Monte Carlo-based method to estimate radiation dose from spiral CT: from phantom testing to patient-specific models. Phys Med Biol 2003;48:2645–63.
[91] Norris H, Zhang Y, Bond J, Sturgeon G, Minhas A, Tward D, et al. A set of 4D pediatric XCAT reference phantoms for multimodality research. Med Phys 2014;41:033701–33711.
[92] Segars W, Norris H, Sturgeon G, Zhang Y, Bond J, Minhas A, et al. The development of a population of 4D pediatric XCAT phantoms for imaging research and optimization. Med Phys 2015;42:4719–26.
[93] Christ A, Kainz W, Hahn E, Honegger K, Zefferer M, Neufeld E, et al. The Virtual Family–development of surface-based anatomical models of two adults and two children for dosimetric simulations. Phys Med Biol 2010;55:23–38.
[94] https://www.aapm.org/pubs/CTProtocols/.
[95] Turner AC, Zankl M, DeMarco JJ, Cagnon CH, Zhang D, Angel E, et al. The feasibility of a scanner-independent technique to estimate organ dose from MDCT scans: using CTDIvol to account for differences between scanners. Med Phys 2010;37:1816–25.
[96] Papadimitroulas P, Erwin WD, Iliadou V, Kostou T, Loudos G, Kagadis GC. A personalized, Monte Carlo-based method for internal dosimetric evaluation of radiopharmaceuticals in children. Med Phys 2018;3939–49.
[97] Visvikis D, Bardies M, Chiavassa S, Danford C, Kirov A, Lamare F, et al. Use of the GATE Monte Carlo package for dosimetry applications. Nucl Instrum Meth Phys Res, Sect A 2006;569:335–40.